

# Phase-transition-induced p-n junction in single halide perovskite nanowire

Qiao Kong<sup>a</sup>, Woonchul Lee<sup>b</sup>, Minliang Lai<sup>a</sup>, Connor G. Bischak<sup>a</sup>, Guoping Gao<sup>c</sup>, Andrew B. Wong<sup>a,c</sup>, Teng Lei<sup>a</sup>, Yi Yu<sup>d</sup>, Lin-Wang Wang<sup>c</sup>, Naomi S. Ginsberg<sup>a,c,e,f,g</sup>, and Peidong Yang<sup>a,c,f,h,1</sup>

<sup>a</sup>Department of Chemistry, University of California, Berkeley, CA 94720; <sup>b</sup>Department of Mechanical Engineering, University of Hawaii at Manoa, Honolulu, HI 96822; <sup>c</sup>Materials Sciences Division, Lawrence Berkeley National Laboratory, Berkeley, CA 94720; <sup>d</sup>School of Physical Science and Technology, ShanghaiTech University, 201210 Shanghai, China; <sup>e</sup>Department of Physics, University of California, Berkeley, CA 94720; <sup>f</sup>Kavli Energy NanoScience Institute, Berkeley, CA 94720; <sup>g</sup>Molecular Biophysics and Integrated Bioimaging Division, Lawrence Berkeley National Laboratory, Berkeley, CA 94720; and <sup>h</sup>Department of Materials Science and Engineering, University of California, Berkeley, CA 94720

Contributed by Peidong Yang, July 26, 2018 (sent for review April 16, 2018; reviewed by Liberato Manna and Yang Yang)

**Semiconductor p-n junctions are fundamental building blocks for modern optical and electronic devices. The p- and n-type regions are typically created by chemical doping process. Here we show that in the new class of halide perovskite semiconductors, the p-n junctions can be readily induced through a localized thermal-driven phase transition. We demonstrate this p-n junction formation in a single-crystalline halide perovskite CsSnI<sub>3</sub> nanowire (NW). This material undergoes a phase transition from a double-chain yellow (Y) phase to an orthorhombic black (B) phase. The formation energies of the cation and anion vacancies in these two phases are significantly different, which leads to n- and p-type electrical characteristics for Y and B phases, respectively. Interface formation between these two phases and directional interface propagation within a single NW are directly observed under cathodoluminescence (CL) microscopy. Current rectification is demonstrated for the p-n junction formed with this localized thermal-driven phase transition.**

halide perovskite nanowire | heterostructure | phase transition | p-n junction | electrical transport

The intensive research impetus on halide perovskite materials, originating from their exceptional progress in solution-processed photovoltaics, has rapidly extended to various optoelectronic applications and fundamental studies due to their abundant elemental compositions and crystal structures as well as many unusual, tunable physical properties (1–10). This is exemplified by all-inorganic halide perovskites, including CsBX<sub>3</sub> (B = Pb, Sn and X = Cl, Br, I). These compositions have attracted increasing attention because of their enhanced ambient stability compared with organic–inorganic hybrid counterparts in which organic cations occupy the Cs site (2, 10). Remarkable features such as efficient charge transport and unique thermoelectric properties have been discovered (8, 11). In addition, phase transitions, giving rise to significant structural reconfiguration without composition change, have been realized mainly via temperature control to establish structure–property correlations (12, 13). However, heterojunction formation in this class of materials is largely unexplored thus far.

Heterojunctions, here referring to solid-state interfaces between two dissimilar materials, present unique functionalities that cannot be obtained from individual components. In particular, with an interface between n- and p-type semiconductors, p-n heterojunctions exhibit efficient charge separation and current rectification, allowing them to be widely utilized in various fields such as energy-related catalysis and microelectronics (14–19). Formation of p-n heterojunctions mainly relies on the intermix of two doped materials into nanoscale domains (15), sequential deposition of one material onto the other (16, 17), chemical doping of starting materials in confined regions (18, 19), etc. Here we develop a strategy to create and control axial p-n heterojunction formation within CsSnI<sub>3</sub> nanowires (NWs) through a thermal-driven localized phase transition. As a result of the

structural reconfiguration, CsSnI<sub>3</sub> NWs undergo the dramatic change of dominant charge carriers from n-type (Y-CsSnI<sub>3</sub>) to p-type (B-CsSnI<sub>3</sub>), where Y is yellow and B is black. Further, we demonstrate the current rectifying functionality of the resulting p-n heterojunction originating from the distinctly different charge-transport properties of these two phases.

One-dimensional Y-CsSnI<sub>3</sub> NWs were synthesized via a low-temperature solution-processed method in which densely stacked NWs with various aspect ratio and rectangular cross-section were obtained (Fig. 1A and *SI Appendix, Fig. S1*). Via a thermal-driven phase transition, structural transformation from Y-CsSnI<sub>3</sub> to B-CsSnI<sub>3</sub> NWs was demonstrated with the color change from yellow to black at around 150 °C (Fig. 1B). As demonstrated in Fig. 1C, X-ray powder diffraction (XRD) characterization confirmed that the phase transition occurred from Y-CsSnI<sub>3</sub> to B-CsSnI<sub>3</sub>. Y-CsSnI<sub>3</sub> possesses a one-dimensional double-chain structure with edge-sharing [SnI<sub>6</sub>]<sup>2−</sup> polyhedra while B-CsSnI<sub>3</sub> crystallizes into an orthorhombic perovskite network (20) (Fig. 1D and *SI Appendix, Fig. S2*). This phase transition is irreversible under the inert environment (N<sub>2</sub> in our case), in that converted B-CsSnI<sub>3</sub> maintains its black phase despite cooling down to the room temperature. We also

## Significance

**Functional semiconductor heterojunctions are fundamental units for building up advanced optoelectronics and circuits. Halide perovskites, representing a new class of semiconductors with soft and reconfigurable ionic bonding, hold promise for a variety of applications because of their many unusual, tunable physical properties. This paper reports the formation of the current-rectifying p-n heterojunction in single-crystalline CsSnI<sub>3</sub> nanowires via localized phase transition between the n-type yellow and p-type black phases. We attribute the distinction of majority carrier types in these two phases to the different formation energies of the cation and anion vacancies. The present approach to heterojunction formation could inspire deeper understanding of phase-transition dynamics and enable precise control over the design of functional heterostructures using halide perovskite building blocks.**

Author contributions: Q.K., M.L., C.G.B., N.S.G., and P.Y. designed research; Q.K., W.L., M.L., C.G.B., G.G., A.B.W., T.L., Y.Y., and L.-W.W. performed research; P.Y. contributed new reagents/analytic tools; Q.K., W.L., M.L., C.G.B., G.G., A.B.W., T.L., Y.Y., L.-W.W., N.S.G., and P.Y. analyzed data; and Q.K., W.L., G.G., L.-W.W., N.S.G., and P.Y. wrote the paper.

Reviewers: L.M., Istituto Italiano di Tecnologia; and Y.Y., University of California, Los Angeles.

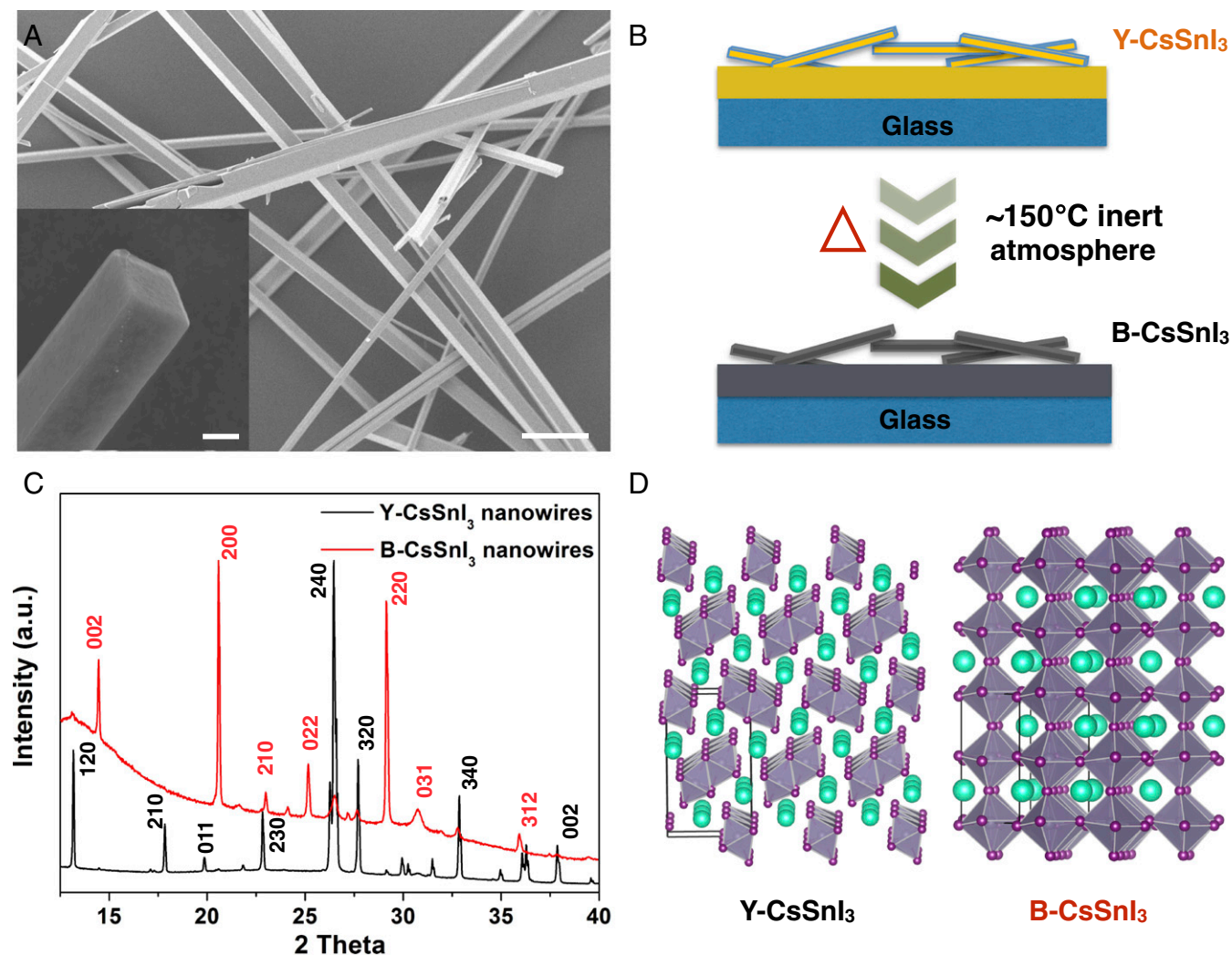
The authors declare no conflict of interest.

Published under the PNAS license.

<sup>1</sup>To whom correspondence should be addressed. Email: p\_yang@berkeley.edu.

This article contains supporting information online at [www.pnas.org/lookup/suppl/doi:10.1073/pnas.1806515115/-DCSupplemental](http://www.pnas.org/lookup/suppl/doi:10.1073/pnas.1806515115/-DCSupplemental).

Published online August 20, 2018.



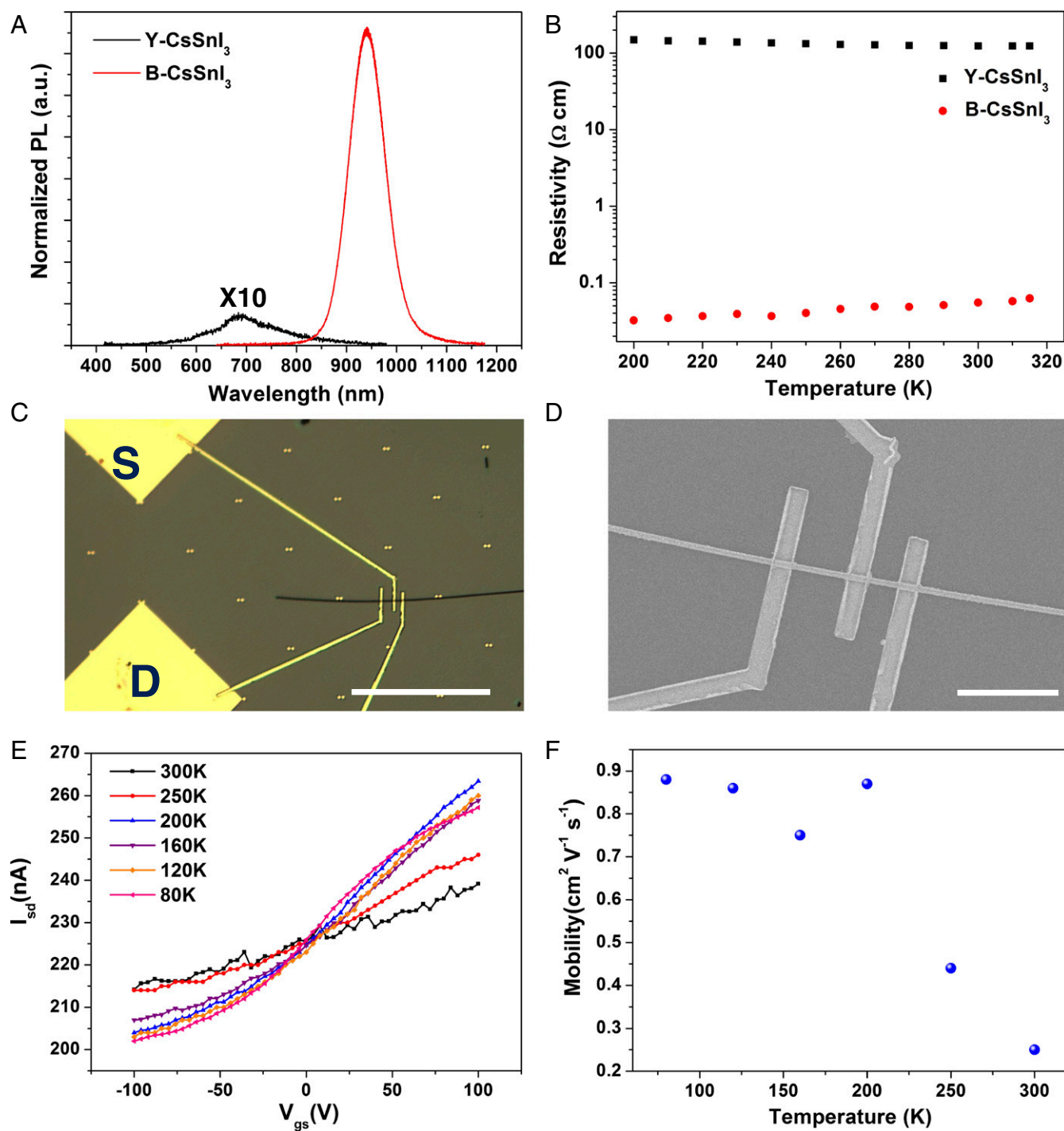


**Fig. 2.** Optical and electrical characterization of single Y- and B-CsSnI<sub>3</sub> NWs. (A) PL spectra of single Y- and B-CsSnI<sub>3</sub> NWs at room temperature. (B) Temperature-dependent electrical resistivity of as-synthesized Y-CsSnI<sub>3</sub> and converted B-CsSnI<sub>3</sub> NWs. (C and D) Optical and SEM image of the fabricated Y-CsSnI<sub>3</sub> NW FET. Back-gate configuration (p<sup>+</sup> Si with  $\rho$  of 0.01–0.05  $\Omega$  cm) was employed with 300-nm-thick SiO<sub>2</sub> atop as dielectric layer. Respectively, 5-nm Ti and 100-nm Pt were sputtered as source and drain contacts. (Scale bars: optical and SEM images, 100 and 5  $\mu$ m, respectively.) (E) A set of transfer characteristics of Y-CsSnI<sub>3</sub> NW FET at various temperatures with  $V_d$  of 0.1 V, suggesting n-type semiconductor behavior. (F) The temperature-dependent field-effect electron mobility measured with source–drain voltage ( $V_d$ ) of 0.1 V.

suppressed at room temperature under various source–drain voltages ( $V_d$ ) (SI Appendix, Fig. S6), which was possibly due to the screening of gate electric field by the migration of ions accumulated at gate dielectric/NW interface (6, 22–24). Thermal activated ion migration reduces as temperature decreases, restoring the evident transfer characteristics and leading to higher

carrier mobility at lower temperature (Fig. 2F). The estimated carrier mobility of  $\sim 0.9$  cm<sup>2</sup> V<sup>−1</sup> s<sup>−1</sup> in Y-CsSnI<sub>3</sub> is about two orders of magnitude smaller than that in B-CsSnI<sub>3</sub> ( $\sim 400$  cm<sup>2</sup> V<sup>−1</sup> s<sup>−1</sup>) (11, 12).

We further identified dominant charge carriers of Y-CsSnI<sub>3</sub> and B-CsSnI<sub>3</sub> to be electrons (n-type) and holes (p-type), respectively, through Seebeck coefficient ( $S$ ) measurement using

suspended microisland devices (25). A known temperature differential was applied between the suspended islands bridged by NW sample, and the open-circuit voltage across the NW was measured (Fig. 3A). The positive sign of  $S$  for B-CsSnI<sub>3</sub> in Fig. 3B revealed its p-type characteristic, while the negative sign of  $S$  for Y-CsSnI<sub>3</sub> confirmed n-type conducting behavior. Theoretical simulation was implemented to explain the difference in majority carriers, which is in general related to dominant intrinsic point defects in the lattice that can donate or accept electrons (12, 26). Because of their relatively low formation energy in the CsSnI<sub>3</sub> lattice, I and Sn vacancies ( $V_{I^+}$  and  $V_{Sn^{2-}}$ ) are suggested to be the most likely shallow defects within the band gap, contributing to free electrons and holes, respectively. Our simulation presents the formation energy of considered defects as a function of Fermi level ( $E_F$ ) under Sn-rich and I-poor conditions (Fig. 3C and *SI Appendix*, Fig. S7). Within each phase, the competition of these two opposite-charged vacancies pins the  $E_F$  at the position where the two formation energy lines cross each other within the band gap between valence band maximum (VBM) and conduction band minimum (CBM). According to our calculations, the preferred  $V_{I^+}$  provides dominant electron carriers in Y-CsSnI<sub>3</sub> so that  $E_F$  is closer to the CBM. On the other hand,  $E_F$  is close to the VBM in B-CsSnI<sub>3</sub>, suggesting the favorable  $V_{Sn^{2-}}$  is the major source for holes. This trend of  $E_F$  shift does agree with the experiments. Furthermore, under thermal equilibrium, the  $E_F$  of Y-CsSnI<sub>3</sub> and B-CsSnI<sub>3</sub> within an NW must align, while also pinned by the crossing of the  $V_{I^+}$  and  $V_{Sn^{2-}}$  formation energies. This will determine the band alignment of the system, leading to a p-n heterojunction, which agrees with experimentally observed current rectification.

The remarkable change in charge-carrier type resulting from the phase transition inspired us to explore p-n heterojunction formation in single CsSnI<sub>3</sub> NW. Combining cathodoluminescence (CL) characterization, which uses a focused electron beam to map the light emission with fine lateral resolution (27), and a sample stage heater, we monitored the distribution of emissive sites caused by the thermal-driven phase transition on individual NWs (*SI Appendix*, Fig. S8A). In situ observation of the NW on a flat silicon substrate showed the emergence of dark-bright segments above the transition temperature, locating n-type Y and p-type B phases within a single NW. Spatially resolved emission mapping across the dark-bright segments confirmed the heterojunction structure, as shown by an abrupt intensity discontinuity at the interface (Fig. 4A). The random appearance of phase-transition segments could result from non-uniform temperature distributions along the NW when attached onto the flat substrate.

To precisely control the phase-transition interface, NWs were next suspended between two elevated pads such that localized phase transition can be initiated from both ends of the NW (Fig. 4B). Our observation showed that the phase transition gradually evolved to the middle of the NW, visualized by the extension of emissive spots (*SI Appendix*, Fig. S8B). Timely cooling allowed the propagation to stop before emissive segments from opposite ends of the NW converged. The junction between the two phases was preserved and the NW was manipulated for electrical characterization. Contacts on the four central electrodes were made in which two were occupied by the p-type bright segment and two by the n-type dark segment (Fig. 4C). Conductance of single-phase segments showed around a 1,000-fold difference, consistent with the result measured on individual Y and B-CsSnI<sub>3</sub> NWs (*SI Appendix*, Fig. S9A). As shown in Fig. 4D, current rectification was obtained across the B-Y interface, which was attributed to the asymmetric p-n heterojunction properties since contact interference was ruled out by the linear and symmetric I-V characteristics of individual phases. To confirm this nonlinear behavior, we performed additional transport measurements through different combinations of electrodes across the junction (*SI Appendix*, Fig. S9B). Positive potentials on the p-type segment reproducibly

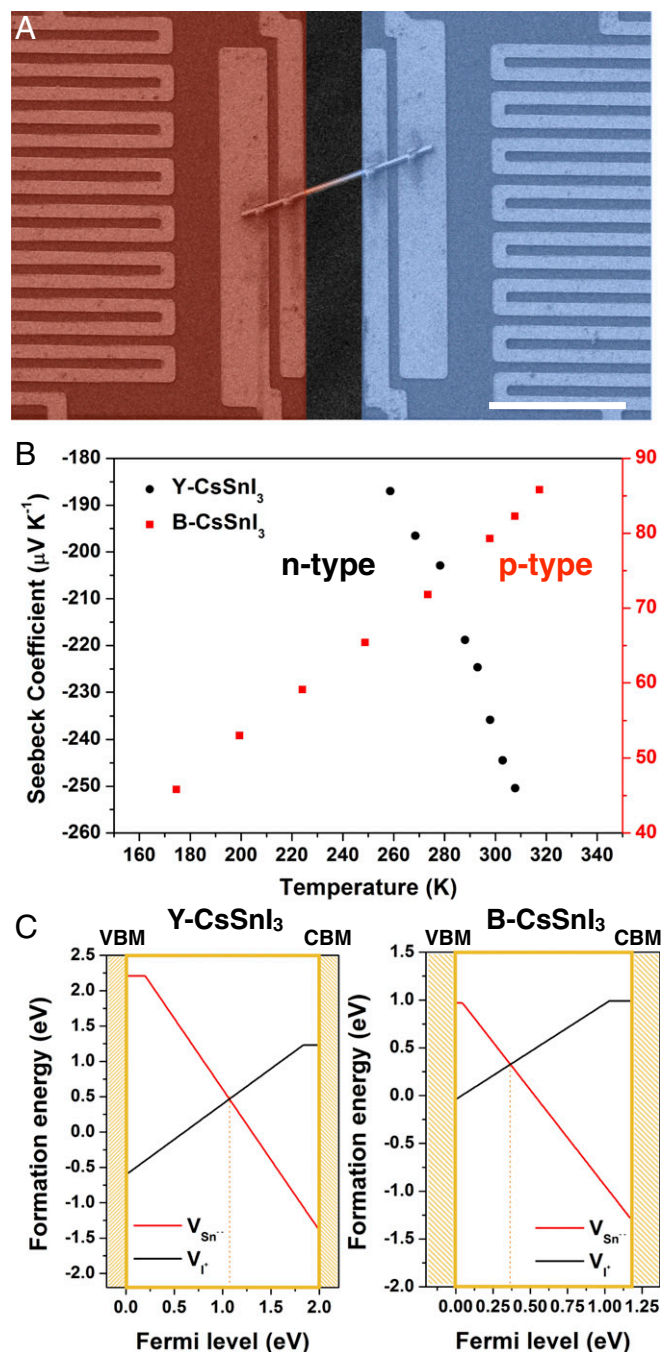


**Fig. 3.** Thermal power measurement and theoretical explanation for distinct majority carrier types in Y-CsSnI<sub>3</sub> and B-CsSnI<sub>3</sub> NWs. (A) SEM image of suspended device for single CsSnI<sub>3</sub> NW Seebeck coefficient measurement. Individual CsSnI<sub>3</sub> NWs transferred on prepatterned platinum electrodes bridged two thermal-isolated islands where temperature gradient was introduced under vacuum conditions (red, hot; blue, cold). (Scale bar: 10  $\mu m$ .) (B) Temperature-dependent Seebeck coefficient of Y-CsSnI<sub>3</sub> and B-CsSnI<sub>3</sub> NWs. Negative Seebeck coefficient implies electrons are the majority carrier in Y-CsSnI<sub>3</sub> NW while positive Seebeck coefficient indicates holes are the majority carrier in B-CsSnI<sub>3</sub> NW. (C) Diagrams of calculated defect formation energies as a function of Fermi level positions for two favorable defects, i.e., Sn and I vacancies, ( $V_{Sn^{2-}}$  and  $V_{I^+}$ ) in the Y- and B-CsSnI<sub>3</sub> under Sn-rich, I-poor condition. As marked in the figure, the energy level of the VBM is set to zero and the CBM is the highest energy of the x axis. The difference between VBM and CBM represents calculated band gap. Crossing point in each plot corresponds to the final pinned position of Fermi level due to the competition of these two vacancy formations at thermal equilibrium.

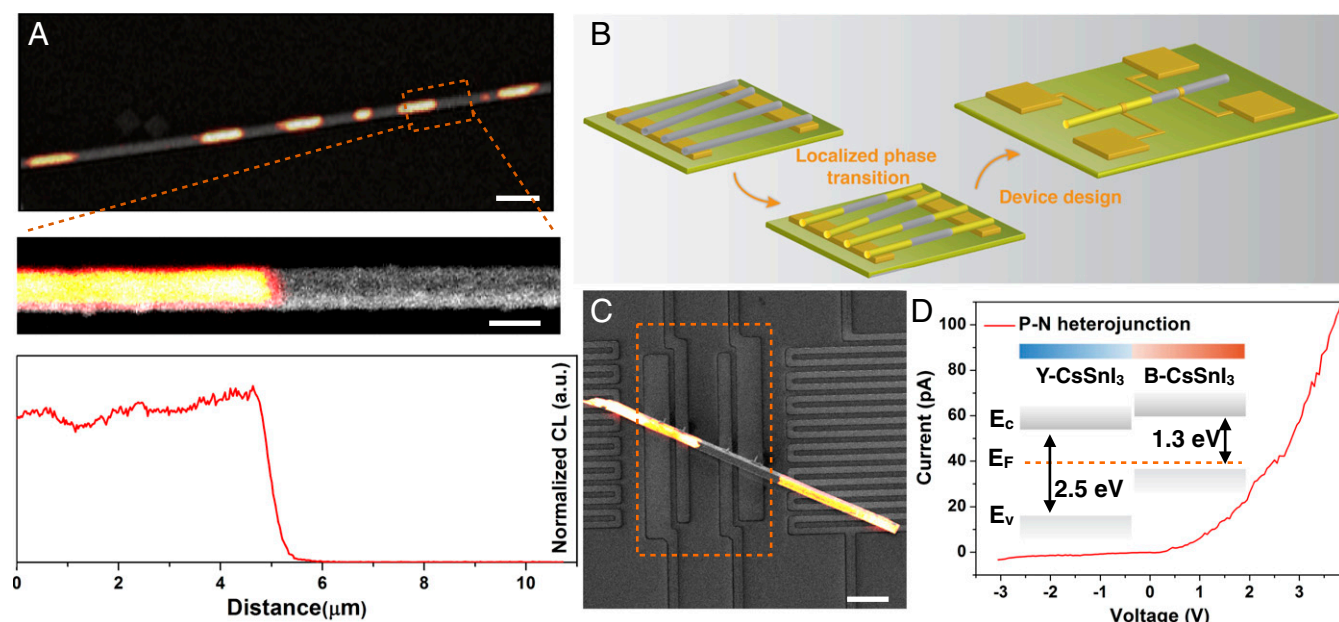


**Fig. 4.** Controllable formation and device characterization of p-n heterojunction in single CsSnI<sub>3</sub> NW through localized phase transition. (A) SEM and CL characterization (715-nm long-pass filter) of localized phase-transition segments randomly distributed along individual CsSnI<sub>3</sub> NWs on flat SiO<sub>2</sub>/Si substrates. Bright signal indicates the completion of the phase transition. (Scale bars: 5 and 1  $\mu$ m, respectively.) (B) Schematic illustration of controllable localized phase transition in single CsSnI<sub>3</sub> NW with two ends on the bottom electrodes. In an ideal situation, two ends of the NW make intimate contact with metal electrodes while the middle of the NW is suspended. With increasing temperature, phase transition initiates at the ends and propagates to the middle along the axial direction. Partially converted NW was preserved when cooling down to room temperature for the device fabrication and characterization. (C) SEM and CL images of CsSnI<sub>3</sub> p-n heterojunction NW device. The central four electrodes (marked with dashed square) were used for electrical measurement. Electron-beam-induced Pt deposition was employed to improve the electrical contact. [Scale bar: (C) 5  $\mu$ m.] (D) I-V characteristics of the p-n heterojunction. (Inset) Energy band alignment of Y-CsSnI<sub>3</sub> and B-CsSnI<sub>3</sub> under thermal equilibrium.

generated increasing current, while applying bias in the opposite direction produced negligible current. Explanation for this unidirectional charge-transport behavior was proposed by the analysis of energy band diagrams of these two phases (Fig. 4D, Inset). Based on the known valence band positions (21) and optical band-gap measurement (SI Appendix, Fig. S10), alignment of Fermi level under thermal equilibrium built up internal charge-transfer barriers. Forward bias (positive potential on B-CsSnI<sub>3</sub>) could overcome the transfer barrier while reverse bias would further enlarge the barrier, leading to anticipated electrical rectifying characteristics.

In conclusion, we have created and characterized p-n heterojunctions in CsSnI<sub>3</sub> NWs via a localized phase transition. We developed a unique method by partially converting the NW from the initial Y phase (n-type) to the B phase (p-type) using heating combined with CL imaging. Understanding the transition of the electronic conduction mechanism associated with the structural transition arouses additional interest for future studies of the phase-transition dynamics. Our approach to phase-engineered NW heterojunctions also provides a universal phase management strategy for the exploration of phase competition and coexistence as well as the interplay of distinct physical properties. Further research on heterojunction structure design to manipulate carrier transport would aid the development of advanced nanoscale optoelectronic devices.

## Materials and Methods

Additional details regarding the materials and methods may be found in SI Appendix.

**Synthesis of Y-CsSnI<sub>3</sub> NWs.** Y-CsSnI<sub>3</sub> NWs were synthesized on glass substrates cleaned with sequential sonication in acetone, 2-propanol, and deionized water. SnI<sub>2</sub> was deposited on the substrates and then reacted with saturated CsI solution (anhydrous 2-propanol). Reactions proceeded in an argon-filled glove box with an oxygen level of <0.1 ppm and a H<sub>2</sub>O level of <0.1 ppm. All

reagents were used as received without further purification. Specifically, saturated solutions of CsI (99.999%, anhydrous beads; Aldrich) in anhydrous 2-propanol (99.5%; Aldrich) was prepared. Then, a small SnI<sub>2</sub> (99.999%, ultradry; Alfa Aesar) particle (~10 mg) was directly put on the clean substrates and the substrate was carefully immersed in a clean 20-mL vial (no. F574504-20; Kimble) with 2 mL CsI/2-propanol. The reaction went for about 12 h at room temperature with the vial carefully capped. The substrate was carefully rinsed clean with anhydrous 2-propanol and dried at 70 °C for 5 min. To minimize air/humidity exposure, the samples were sealed in the centrifuge tubes and stored in the glove box with an O<sub>2</sub> level <0.1 ppm and a H<sub>2</sub>O level <0.1 ppm.

**Characterization of CsSnI<sub>3</sub> NWs.** Scanning electron microscopic (SEM) images of as-synthesized Y-CsSnI<sub>3</sub> NWs and converted B-CsSnI<sub>3</sub> NWs were acquired using a JEOL JSM-6340F field-emission SEM. A Zeiss 1540 EsB instrument was used to take SEM images of single-NW devices and for electron-beam-induced deposition of platinum. Transmission electron microscopy, energy-dispersive X-ray spectroscopy mapping were collected on an FEI Titan microscope at 300 keV at the National Center for Electron Microscopy. The absorption measurement was carried out on a Shimadzu UV-2550 UV-vis-near-IR spectrophotometer with an integrating sphere. PL was collected using 405-nm excitation from a laser diode on a Nikon A1 microscope coupled to a multimode fiber and the spectra were obtained with a liquid-nitrogen-cooled UV-vis spectrometer (Princeton Instruments/Acton) for Y-CsSnI<sub>3</sub> and InGaAs CCD (PI Acton) for B-CsSnI<sub>3</sub>. CL images were acquired with a modified Zeiss Gemini SUPRA 55 SEM. The emission images were collected using photon-counting module (SPCM-AQR-15; Perkin-Elmer) with a 700-nm long-pass filter.

**Electrical and Thermal Power Measurement.** Electrical conductivity and thermal power measurements were performed on a reported delicate single-NW prepatterned device (25). Individual CsSnI<sub>3</sub> NWs were placed using a manipulator across two electrically and thermal-isolated microislands. The device substrate was transferred to a closed-cycle He cryostat (Janis). For thermal power measurement, the temperature differential across the NW was created through Joule heating under high vacuum (<10<sup>-6</sup> torr), and voltage differential across the NW was acquired. Four-probe resistance was

obtained using a current source (Keithley 6221) and nanovoltmeter (Keithley 2182) under vacuum at different temperature points. Temperature-dependent FET device measurements were carried out in a probe station under vacuum coupled with a source/measurement unit (Keithley 2636A).

**Theoretical Simulation.** The electronic structure calculations were performed by using density-functional theory as implemented in the Vienna Ab initio Simulation Package code (28, 29). The exchange-correlation interactions were described by the generalized gradient approximation in the form of the Perdew–Burke–Ernzerhof functional (30, 31). The defect calculation was based on  $2 \times 2 \times 2$ ,  $1 \times 4 \times 2$  supercell for black phase and yellow phase  $\text{CsSnI}_3$ , respectively, which includes 160 atoms. The K point is set to  $2 \times 2 \times 2$ . In all calculations, all of the atoms are allowed to relax until all of the forces on atoms are below 0.05 eV/Å.

**ACKNOWLEDGMENTS.** We are grateful to Dr. L. Dou, Dr. D. Zhang, and Dr. Y. Yang for fruitful discussions. We thank Ed Wong from the Molecular Foundry for assistance with the CL-compatible heater stage, and Ed Barnard,

Shaul Aloni, and Frank Ogletree for their stewardship of the CL facilities. We are grateful for the nanofabrication and imaging facilities in Marvell Nanofabrication Laboratory and Molecular Foundry. This work was supported by the US Department of Energy, Office of Science, Office of Basic Energy Sciences, Materials Sciences and Engineering Division, under Contract DE-AC02-05CH11231 within the Physical Chemistry of Inorganic Nanostructures Program (KC3103). Transmission electron microscopy and CL characterization were carried out at the National Center for Electron Microscopy and Molecular Foundry, supported by the Office of Science, Office of Basic Energy Science, of the US Department of Energy under Contract DE-AC02-05CH11231. CL characterization was supported by a David and Lucile Packard Fellowship for Science and Engineering to N.S.G. and by STROBE, a National Science Foundation Science and Technology Center under Grant DMR 1548924. The theoretical work in this research used the resources of the National Energy Research Scientific Computing Center that is supported by the Office of Science of the US Department of Energy. Q.K., M.L., and T.L. acknowledge the graduate fellowship from Suzhou Industrial Park. C.G.B. acknowledges an NSF Graduate Research Fellowship (DGE 1106400). A.B.W. acknowledges the support of the Lam Research Fellowship.

1. Stoumpos CC, Kanatzidis MG (2015) The renaissance of halide perovskites and their evolution as emerging semiconductors. *Acc Chem Res* 48:2791–2802.
2. Niu G, Guo X, Wang L (2015) Review of recent progress in chemical stability of perovskite solar cells. *J Mater Chem A* 3:8970–8980.
3. Docampo P, Bein T (2016) A long-term view on perovskite optoelectronics. *Acc Chem Res* 49:339–346.
4. Stoumpos CC, Malliakas CD, Kanatzidis MG (2013) Semiconducting tin and lead iodide perovskites with organic cations: Phase transitions, high mobilities, and near-infrared photoluminescent properties. *Inorg Chem* 52:9019–9038.
5. Swarnkar A, et al. (2016) Quantum dot-induced phase stabilization of  $\alpha$ - $\text{CsPbI}_3$  perovskite for high-efficiency photovoltaics. *Science* 354:92–95.
6. Li D, et al. (2016) Size-dependent phase transition in methylammonium lead iodide perovskite microplate crystals. *Nat Commun* 7:11330.
7. Dou L, et al. (2015) Atomically thin two-dimensional organic-inorganic hybrid perovskites. *Science* 349:1518–1521.
8. Chung I, Lee B, He J, Chang RP, Kanatzidis MG (2012) All-solid-state dye-sensitized solar cells with high efficiency. *Nature* 485:486–489.
9. Cho H, et al. (2015) Overcoming the electroluminescence efficiency limitations of perovskite light-emitting diodes. *Science* 350:1222–1225.
10. Eaton SW, et al. (2016) Lasing in robust cesium lead halide perovskite nanowires. *Proc Natl Acad Sci USA* 113:1993–1998.
11. Lee W, et al. (2017) Ultralow thermal conductivity in all-inorganic halide perovskites. *Proc Natl Acad Sci USA* 114:8693–8697.
12. Chung I, et al. (2012)  $\text{CsSnI}_3$ : Semiconductor or metal? High electrical conductivity and strong near-infrared photoluminescence from a single material. High hole mobility and phase-transitions. *J Am Chem Soc* 134:8579–8587.
13. Lai M, et al. (2017) Structural, optical and electrical properties of phase-controlled cesium lead iodide nanowires. *Nano Res* 10:1107–1114.
14. Liu Y, et al. (2016) Van der Waals heterostructures and devices. *Nat Rev Mater* 1:16042.
15. Park S, et al. (2009) Bulk heterojunction solar cells with internal quantum efficiency approaching 100%. *Nat Photonics* 3:297–302.
16. Liu C, Tang J, Chen HM, Liu B, Yang P (2013) A fully integrated nanosystem of semiconductor nanowires for direct solar water splitting. *Nano Lett* 13:2989–2992.
17. Li M-Y, et al. (2015) NANOELECTRONICS. Epitaxial growth of a monolayer  $\text{WSe}_2$ - $\text{MoS}_2$  lateral p-n junction with an atomically sharp interface. *Science* 349:524–528.
18. Sze SM, Ng KK (2007) *Physics of Semiconductor Devices* (Wiley, Hoboken, NJ).
19. Ci L, et al. (2010) Atomic layers of hybridized boron nitride and graphene domains. *Nat Mater* 9:430–435.
20. Yamada K, et al. (1991) Structural phase transitions of the polymorphs of  $\text{CsSnI}_3$  by means of Rietveld analysis of the X-ray diffraction. *Chem Lett* 20:801–804.
21. Zhang J, et al. (2014) Energy barrier at the  $\text{N719-dye/CsSnI}_3$  interface for photo-generated holes in dye-sensitized solar cells. *Sci Rep* 4:6954–6959.
22. Yuan Y, Huang J (2016) Ion migration in organometal trihalide perovskite and its impact on photovoltaic efficiency and stability. *Acc Chem Res* 49:286–293.
23. Li F, et al. (2015) Ambipolar solution-processed hybrid perovskite phototransistors. *Nat Commun* 6:8238.
24. Li D, et al. (2017) Gate-induced insulator to band-like transport transition in organolead halide perovskite. *J Phys Chem Lett* 8:429–434.
25. Lee J, et al. (2016) Thermal transport in silicon nanowires at high temperature up to 700 K. *Nano Lett* 16:4133–4140.
26. Yin W-J, Shi T, Yan Y (2014) Unusual defect physics in  $\text{CH}_3\text{NH}_3\text{PbI}_3$  perovskite solar cell absorber. *Appl Phys Lett* 104:063903.
27. Bischak CG, Sanehira EM, Precht JT, Luther JM, Ginsberg NS (2015) Heterogeneous charge carrier dynamics in organic-inorganic hybrid materials: Nanoscale lateral and depth-dependent variation of recombination rates in methylammonium lead halide perovskite thin films. *Nano Lett* 15:4799–4807.
28. Kresse G, Furthmüller J (1996) Efficiency of ab-initio total energy calculations for metals and semiconductors using a plane-wave basis set. *Comput Mater Sci* 6:15–50.
29. Kresse G, Furthmüller J (1996) Efficient iterative schemes for ab initio total-energy calculations using a plane-wave basis set. *Phys Rev B Condens Matter* 54:11169–11186.
30. Perdew JP, Burke K, Ernzerhof M (1996) Generalized gradient approximation made simple. *Phys Rev Lett* 77:3865–3868.
31. Perdew JPM, Ernzerhof M (1996) Rationale for mixing exact exchange with density functional approximations. *J Chem Phys* 105:9982–9985.